

Reversible hydrogen storage properties of defect-engineered C₄N nanosheets under ambient conditions

Khidhir Alhameedi ^{a,*}, Tanveer Hussain ^{a,**}, Hyeonhu Bae ^b, Dylan Jayatilaka ^a, Hoonkyung Lee ^b, Amir Karton ^a

^a School of Molecular Sciences, The University of Western Australia, Perth, WA, 6009, Australia

^b Department of Physics, Konkuk University, Seoul, 05029, Republic of Korea

ARTICLE INFO

Article history:

Received 18 April 2019

Received in revised form

27 May 2019

Accepted 29 May 2019

Available online 3 June 2019

Keywords:

Nanosheet

Dopant

Adsorption

Desorption

Storage capacity

Defects

Bonding nature

ABSTRACT

Inspired by the promise of hydrogen (H₂) as a clean alternate to the existing energy sources, we have employed spin-polarized density functional theory calculations on a recently designed two-dimensional C₄N monolayer as a promising H₂ storage material. By means of first principles DFT calculations, we have comprehensively studied the geometric and electronic properties of pristine, defected and metal-doped C₄N nanosheets and further explored their H₂ storage properties. We found that light metal dopants such as Li, Na, K, Mg, and Ca bind strongly to defects on a C₄N nanosheet with binding energies of 3–4 eV per dopant. These binding energies are sufficiently strong to surpass metal clustering. Thermal stability of the metal-doped C₄N nanosheets has been further verified by means of ab initio molecular dynamics simulations. The bonding nature of the metal dopants with the C₄N nanosheet has been studied through Bader analysis and Roby-Gould methods and the electronic properties were studied through density of states. We found that each dopant in the metal-doped C₄N nanosheet can bind up to five H₂ molecules with adsorption energies ranging between 0.15 and 0.60 eV/H₂, which results in optimal H₂ storage capacities. Finally, we employed thermodynamic analysis to investigate the H₂ adsorption/desorption mechanism under practical operating conditions.

© 2019 Elsevier Ltd. All rights reserved.

1. Introduction

Aside from diminishing availability and geopolitical challenges, the use of fossil fuels results in environmental and health concerns which could be alleviated by replacing the current energy sources with cleaner, renewable and efficient alternatives [1]. Hydrogen (H₂) is one such energy carrier that could substitute fossil fuels due to its high energy content, environmental friendliness, abundance and renewable nature [2,3]. Nevertheless, an efficient storage medium is essential for realizing the H₂ economy. Although liquefaction and pressure-induced H₂ storage has been employed, energy cost and safety issues related with these methods make them unviable for large scale applications [4,5]. Solid-state material based H₂ storage is another option to explore; however the pursuit of such promising materials, which can accommodate a large amount

of H₂ and release it when needed at practical operating conditions, is a critical barrier that needs to be overcome [6,7]. For efficient storage, the binding energy of H₂ with the host material should lie within a range of –0.15 to –0.60 eV, to enable adsorption/desorption within suitable operating conditions [8,9]. Moreover the H₂ gravimetric density should be at least 5.5 wt%, as per Department of Energy (DOE) guidelines, which makes low-dimensional light materials a promising storage option [10].

Two-dimensional (2D) nanostructures are undoubtedly one of the most studied classes of materials due to their unique properties, which are very different from their bulk morphologies [11,12]. Thanks to their lightweight and large surface to volume ratio, 2D materials have found their promise in numerous applications including H₂ storage [13–15]. However, the binding enthalpies of H₂ with the majority of 2D materials (in their pure form) fall under weak physisorption, which diminish the H₂ storage capacities and allow their operation only at very low temperatures, hence not applicable for real world applications. Therefore, the adsorption energies between H₂ and the host materials need to be enhanced to facilitate adsorption and desorption at feasible storage conditions.

* Corresponding author.

** Corresponding author.

E-mail addresses: khidhir.abdalhussein@gmail.com (K. Alhameedi), tanveersaram@gmail.com (T. Hussain).

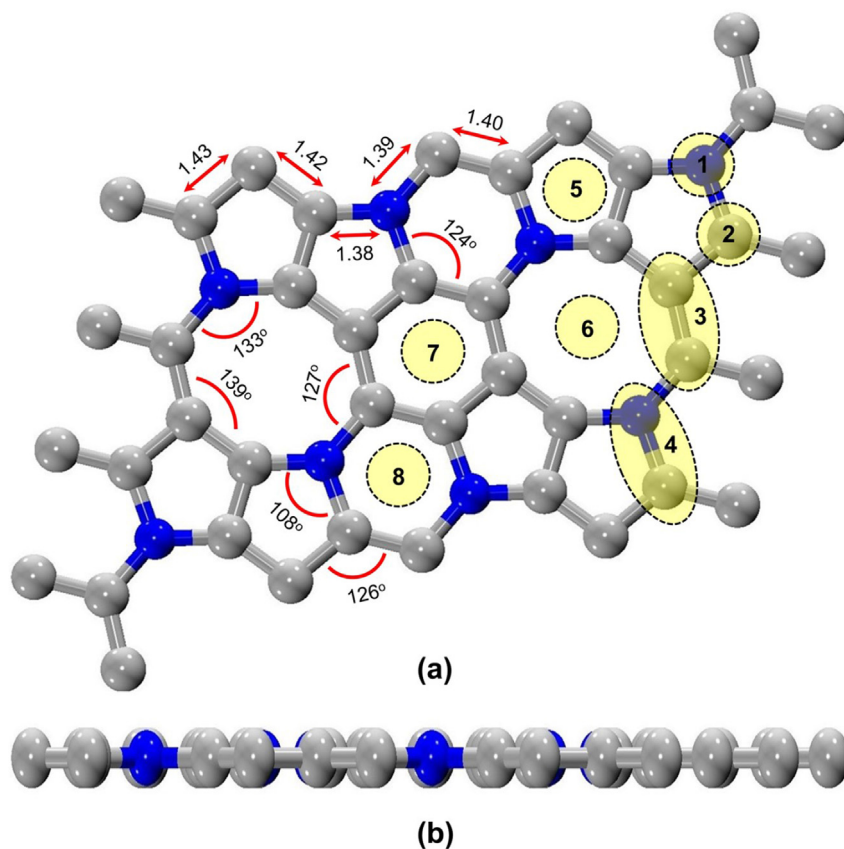


Fig. 1. Top and side views of optimized structures for C_4N nanosheet. Selected bond lengths (in Å) and angles (in degrees). The highlighted areas are possible metal adsorption sites over the (1) N atom, (2) C atom, (3) C – C bridge, (4) C – N bridge, and (5)–(7) hollow sites of the different rings. Atom colors: C-gray, and N-blue. (A colour version of this figure can be viewed online.)

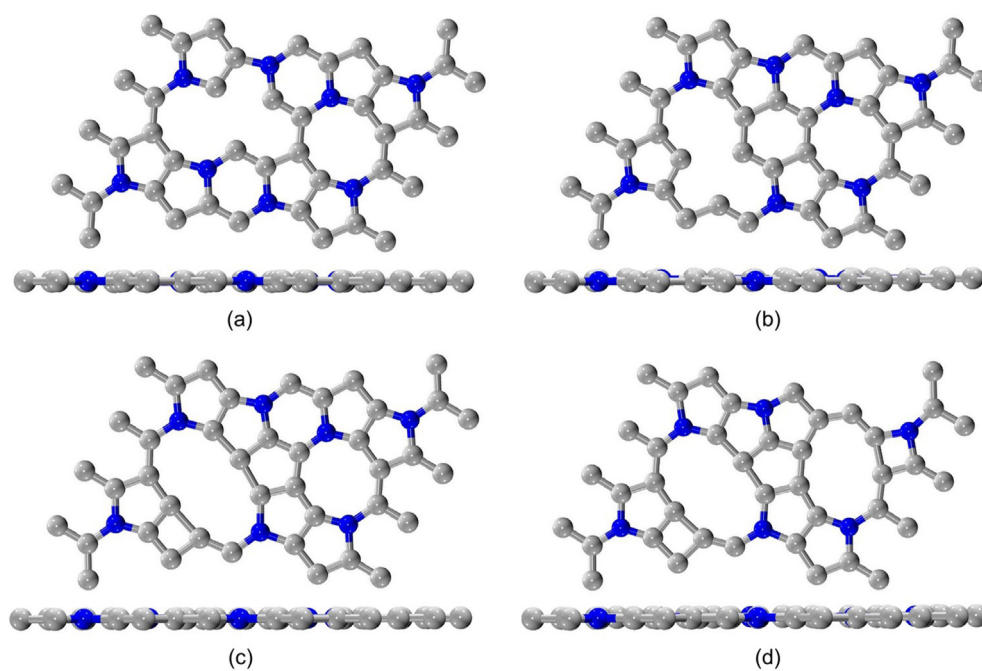


Fig. 2. Top and side views of the optimized structures of defected C_4N nanosheet for (a) C-vacancy, (b) N-vacancy, (c) di-vacancy (C and N), and (d) quad-vacancy (2C and 2N). Atom colors: C-gray and N-blue. (A colour version of this figure can be viewed online.)

One of the most studied approaches in improving H_2 enthalpies is the decoration of the host 2D material surfaces with elements (or clusters) of alkali, alkaline or transition metals [16–23]. Many theoretical as well as experimental studies have shed light on metal decorated 2D nanostructures as promising H_2 storage materials.

On the experimental end, Zhou et al. designed a composite of Ni-graphene, by distributing Ni nanoparticles of length 10 nm on graphene monolayer and studied its H_2 storage properties at practical temperature and pressure ranges. It was demonstrated that H_2 gravimetric density could be enhanced from 0.1 wt% to 1.18 wt% upon the increment in pressure from 1 to 60 bar, respectively [24]. The same group further developed a system by distributing Pd clusters of 5–45 nm in size over a graphene surface and obtained a much higher H_2 content of 6.7 wt% at a pressure of 50 bar. When the applied pressure reached 60 bar, an even higher H_2 gravimetric density of 8.67 wt% was obtained [20].

Hashmi et al. studied H_2 storage properties of recently synthesized Nitrogenated holey graphene (C_2N) by doping it with Li adatoms by means of DFT calculations [25]. It was reported that the Li dopants made strong bonds with the C_2N monolayers and dispersed uniformly over the surface without being clustered. A significantly high H_2 storage capacity could be achieved with appropriate binding energies that ensure adsorption/desorption at feasible fuel cell operating conditions [25]. Very recently Luo et al. used DFT calculations on an experimentally synthesized blue phosphorene monolayer under Li doping for H_2 storage applications. It was reported that Li dopants could form 1:1 P/Li doping concentrations and reached H_2 storage capacity of 9.52 wt% with adsorption energy of -0.168 eV/ H_2 [26]. Wang et al. studied the structural and H_2 storage properties of 2D boron sheet upon functionalization with Ca metals through first principles

calculations. These authors concluded that each Ca dopant could anchor a maximum of 6 H_2 molecules with an average adsorption energy range of -0.2 to -0.32 eV/ H_2 , which fall within the desired range [27].

A very recent addition to the family of 2D materials is graphitic carbon nitride nanosheet, C_4N , which was designed through global structure search approach and found stable both thermally and dynamically [28]. In addition to the other promising properties, C_4N has an intrinsic bandgap, which makes it a fascinating material for nanoelectronics. Motivated by these intriguing properties, we have studied the structural, electronic and H_2 storage properties of vacancy induced metallized C_4N nanosheet. We found that under vacancy defects, C_4N bind several light metal dopants, which could be used as high capacity H_2 storage materials.

2. Computational details

Spin-polarized density functional theory (DFT) calculations were performed using the VASP code [29–31]. We used the generalized gradient approximation (GGA) and projector-augmented wave method (PAW) for exchange-correlation and electron-ion interactions [32,33]. Considering the weak interactions between H_2 and the metal systems, we used the DFT-D3 empirical dispersion correction of Grimme and co-workers [34]. Cut-off energy of 500 eV was used for the plane-wave basis set. A vacuum space of 18 Å was inserted along z-direction to avoid the interaction between the periodic images. We used Monkhorst-Pack scheme for the Brillouin zone at $5 \times 5 \times 1$ for optimization and much denser mesh of $9 \times 9 \times 1$ for density of states (DOS) [35]. All the systems were optimized until convergence and force criteria of 10 -6 eV and 0.01 eV/Å, respectively were met. Charge transfer mechanism was studied by employing Bader analysis [36] and Roby-Gould method [40–42].

3. Results and discussion

We begin with studying the structural properties of a pristine C_4N nanosheet, including bond lengths, bond angles, and lattice parameters. Fig. 1 shows the optimized structure of the pure C_4N nanosheet and geometric parameters. The optimized structure of C_4N consists of five-, six-, and eight-membered rings. The five-membered rings contain one heteroatom whereas the six- and eight-membered rings contain two heteroatoms. The bond lengths of C–C and C–N are found to be in the range of 1.40–1.43 and 1.38–1.40 Å, respectively. The lattice parameters are $a = 9.67$ Å and $b = 11.91$ Å. The structural parameters are in good agreement with a previous DFT study of C_4N nanosheets [28].

As expected, the binding energy of H_2 molecules on the pure C_4N nanosheet are much smaller than the desired binding energy range.

Thus, pristine C_4N nanosheet cannot be used for H_2 storage applications, unless H_2 binding is enhanced. Among various available options, metal doping on 2D materials is an extensively employed approach for increasing the H_2 binding energies. Therefore, we have introduced light metals (M), which are Li, Na, K, Mg, and Ca, on the C_4N nanosheet. The reasons of selecting these light metals are: (1) the high ratios of their binding to cohesive energies help these metals disperse uniformly over the C_4N nanosheet without being clustered and (2) light metal dopants are expected to result in significantly high storage capacities. To locate the lowest energy configurations, the addition of a single M dopant on eight possible adsorption positions over the C_4N nanosheet have been considered (these positions are highlighted in yellow in Fig. 1). In order to determine the most favourable site of M dopants, we

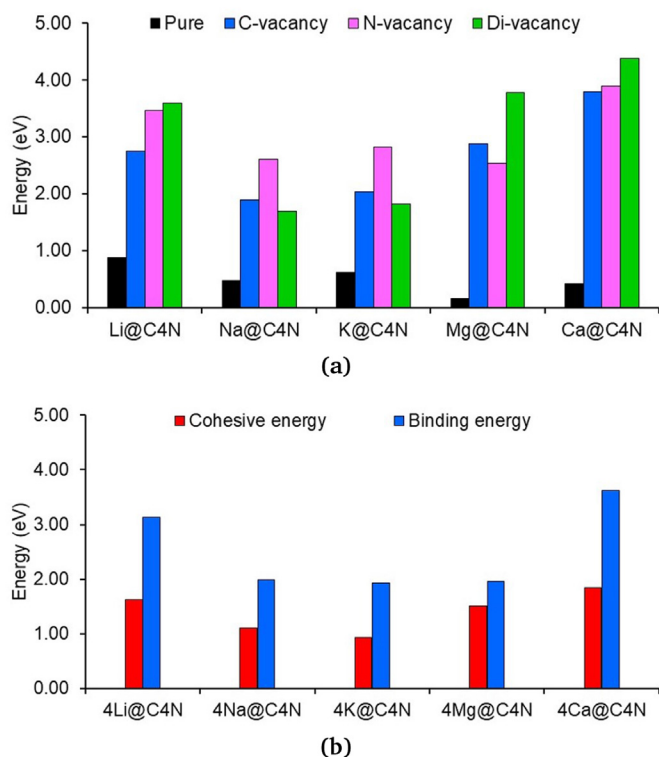


Fig. 3. Binding energies per M (Li, Na, K, Mg, and Ca) for (a) mono doping on non-defected (pure), and defected C_4N systems, and (b) for maximum doping on C_4N ($^{2C/2N}$ quad-vacancy) systems, calculated using DFT-D3. For clarity the absolute values of the binding energies were plotted. (A colour version of this figure can be viewed online.)

calculated the binding energy E_b^M for each of the eight positions, which are above the N and C atoms, C–C and C–N bonds, and center of the four ring types, as follows:

$$E_b^M = E_{M@C_4N} - E_{C_4N} - E_M. \quad (1)$$

Where E_{C_4N} , E_M and $E_{M@C_4N}$ are the total energies of C_4N , M , and M decorated C_4N , respectively. The results demonstrate that the energetically most preferable binding site is the center of the hexagonal ring (site 7, Fig. 1). The binding energies (E_b^M) to this position are: 0.88, 0.48, 0.62, 0.16, and 0.42 eV for $Li@C_4N$, $Na@C_4N$, $K@C_4N$, $Mg@C_4N$, and $Ca@C_4N$, respectively. However, these binding energies are lower than the corresponding cohesive energies E_c of the M dopants, which are 1.63, 1.11, 0.93, 1.51, and 1.84 eV/atom, for Li, Na, K, Mg, and Ca, respectively. This situation would lead to metal clustering (i.e. $E_b/E_c < 1$) rather than M – C_4N binding (i.e. $E_b/E_c > 1$). In order to avoid metal clustering the M – C_4N binding energies have to be enhanced.

Defect formation is one of the most efficient techniques to

improve the binding of metal dopants to 2D surfaces [22,37,38]. We, therefore, consider the following defects: (1) C-vacancy (C_4N^{-C}), (2) N-vacancy (C_4N^{-N}), (3) di-vacancy (C/N) ($C_4N^{-C/N}$), and (4) quad-vacancy (2C/2N) ($C_4N^{-2C/2N}$). It is worth mentioning that different C vacancies were considered and the one with the lowest total energy was considered for metal doping. Before discussing the binding mechanism of M on these defects, we will briefly describe the structural properties of these systems. Fig. 2a–c shows the

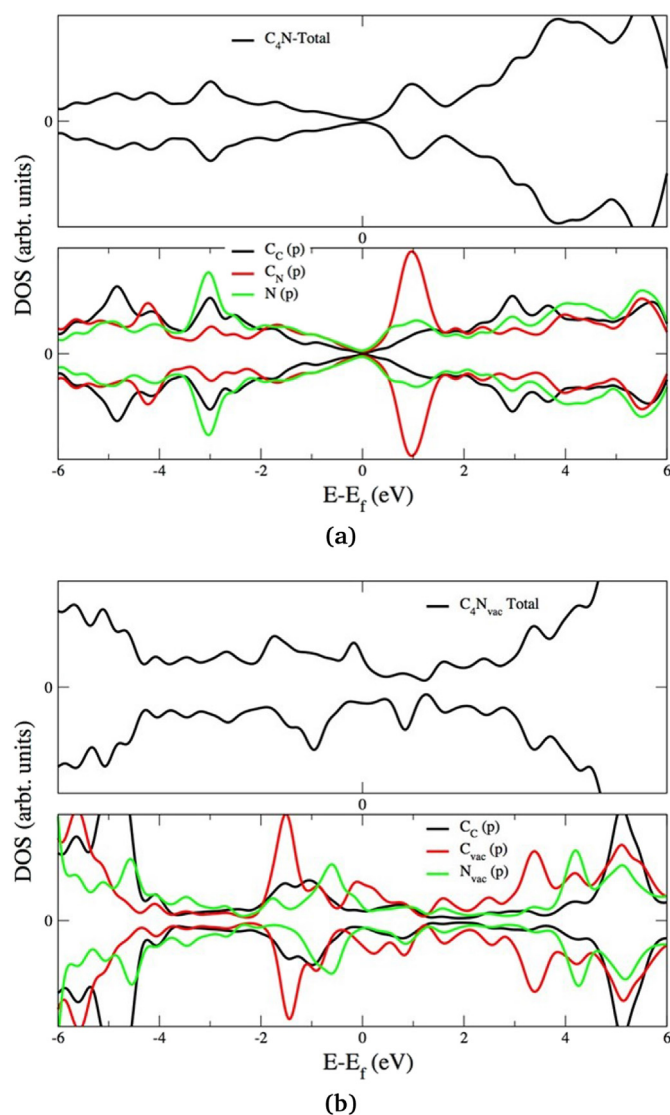


Fig. 4. Total and partial density of states of (a) pristine C_4N nanosheet, and (b) quad-vacancy $C_4N^{-2C/2N}$ system. Fermi level is located at zero. (A colour version of this figure can be viewed online.)

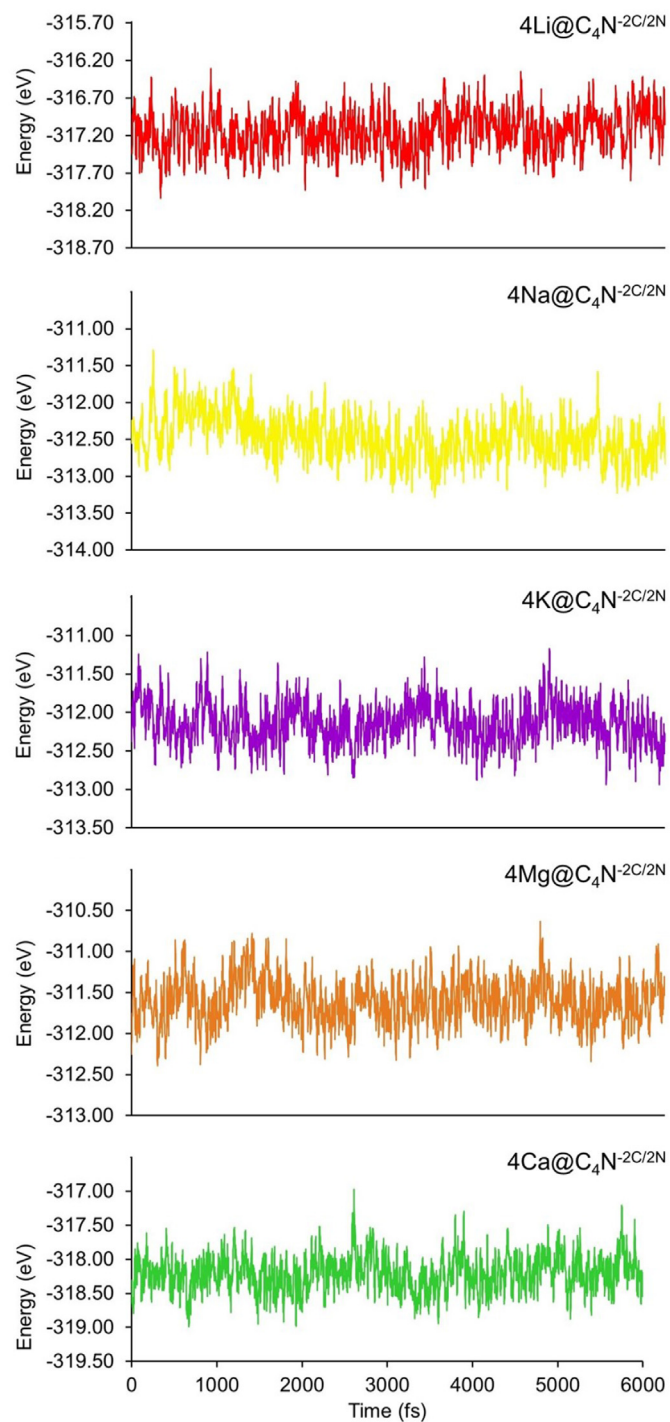


Fig. 5. Molecular dynamics (MD) simulations for metal-functionalized quad-vacancy systems at maximum doping concentration ($4M@C_4N^{-2C/2N}$) at $T = 300$ K. (A colour version of this figure can be viewed online.)

optimized structures of C-vacancy, N-vacancy, di-vacancy, and quad-vacancy C_4N nanosheets, respectively. We find that there is a considerable change in the bond lengths when going from the pure C_4N nanosheet to defected C_4N systems. The C–C bond length ranges are: 1.35–1.45, 1.39–1.46, 1.39–1.77, and 1.38–1.62 for C-vacancy, N-vacancy, di-vacancy, and quad-vacancy, respectively. Whereas C–N bond lengths are found to be in the range of 1.36–1.44, 1.37–1.42, 1.35–1.48, and 1.35–1.48 for C-vacancy, N-vacancy, di-vacancy, and quad-vacancy, respectively. These results generally indicate that the bond lengths are elongated upon increasing the defect concentrations.

In order to examine the effect of structural defects on the E_b^M , and consequently on H_2 adsorption, we introduced a single M on the defected C_4N nanosheets. We calculate E_b^M (per dopant) for each system using the following equation:

$$E_b^M = \frac{E_{nM@C_4N} - E_{C_4N} - nE_M}{n}, \quad (2)$$

where n is the number of dopants, and E_{C_4N} , nE_M , and $E_{nM@C_4N}$ represent the total energy of vacancy induced C_4N , M dopants, and vacancy induced C_4N loaded with M dopants, respectively. Fig. 3a presents the binding energies per M dopant for pure and defected systems. In the case of C-vacancy, the calculated E_b^M energies are: 2.75, 1.90, 2.03, 2.88, and 3.79 eV for $Li@C_4N^{-C}$, $Na@C_4N^{-C}$, $K@C_4N^{-C}$, $Mg@C_4N^{-C}$, and $Ca@C_4N^{-C}$, respectively. Compared to the binding energies with pure C_4N , these E_b^M values are larger by 2.1, 3.0, 2.3, 17.4, and 8.1 times, for Li, Na, K, Mg, and Ca dopants, respectively. The optimized distances of $M-C_4N^{-C}$ are found to be 1.93, 2.26, 2.60, 1.98, and 2.18 Å for Li, Na, K, Mg, and Ca dopants, respectively. For N-vacancy, the E_b^M values of 3.47, 2.61, 2.82, 2.54,

and 3.90 eV were obtained for Li, Na, K, Mg, and Ca dopants, respectively. Compared to pure C_4N , these binding energies are stronger by 3.0, 4.4, 3.6, 15.2, and 8.3 times for Li, Na, K, Mg, and Ca dopants, respectively. The $M-C_4N^{-N}$ optimized distances were found to be 1.97, 2.34, 2.69, 2.00, and 2.28 Å for Li, Na, K, Mg, and Ca dopants, respectively. For di-vacancy, the E_b^M values are 3.60, 1.69, 1.82, 3.78, and 4.38 eV for $Li@C_4N^{-C/N}$, $Na@C_4N^{-C/N}$, $K@C_4N^{-C/N}$, $Mg@C_4N^{-C/N}$, and $Ca@C_4N^{-C/N}$, respectively, which are 3.1, 2.5, 2.0, 23.1, and 9.5 times higher than pure C_4N . The $M-C_4N$ distances of 2.08, 2.40, 2.73, 2.10, and 2.40 Å, were observed for Li, Na, K, Mg, and Ca dopants, respectively. Based on the above structural analysis, it is clear that the binding of $M-C_4N$ has been significantly improved upon the creation of vacancy defects, and in the majority of cases, di-vacancy shows the largest enhancement of the M binding. This motivates us to increase the M doping concentration on the di-vacancy systems.

For the second M doping, the optimized geometries of di-vacancy for the single M decorated $C_4N^{-C/N}$ were used as initial structures. The second dopant was placed close to the vacancy (*i.e.* localized doping) on the opposite side of the first M dopant. Equation (2) was used to calculate the E_b^M of the second dopant. The average E_b^M per M dopant was found to be 3.43, 3.16, 2.70, 2.39, and 4.82 eV, for Li, Na, K, Mg, and Ca, respectively. These E_b^M values are significantly higher than the corresponding E_c values. We therefore, proceed to further increase the M concentration over the di-vacancy system.

To introduce the third M adatom, the di-vacancy $C_4N^{-C/N}$ nanosheets bonded with two metals were used as initial geometries. Now, the third M dopant was introduced at a reasonable distance from the existing M dopants present on either side of the

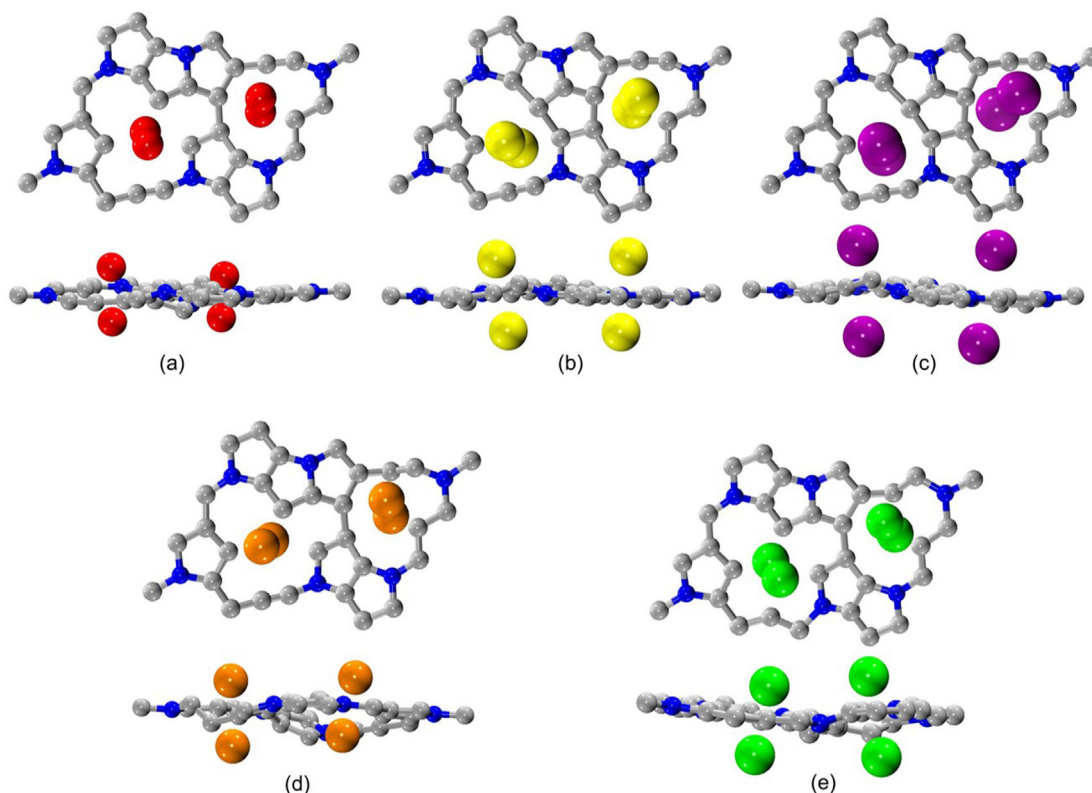


Fig. 6. Top and side views of optimized structures for (a) $4Li@C_4N^{-2C/2N}$, (b) $4Na@C_4N^{-2C/2N}$, (c) $4K@C_4N^{-2C/2N}$, (d) $4Mg@C_4N^{-2C/2N}$, and (e) $4Ca@C_4N^{-2C/2N}$. Atom colors: C-gray, N-blue, Li-red, Na-yellow, K-purple, Mg-orange, and Ca-green. (A colour version of this figure can be viewed online.)

di-vacancy defect. The reason for this is to avoid the electrostatic repulsion among the cationic M center. Introducing the third M away from the vacancy defect would also help to understand the range of vacancy defects in enhancing the binding mechanism. In this case, the values of average E_b^M per M dopant were found as 1.34, 0.84, 0.94, 0.23, and 0.36 eV, for Li, Na, K, Mg, and Ca, respectively. It is evident from the small values of E_b^M , as compared to their corresponding E_c energies, that these defects have a localized effect on the M - C_4N binding. This situation motivated us to enhance the vacancy concentrations, thus we considered another di-vacancy in the super cell of the considered C_4N nanosheet. Hereinafter, we refer to these defects as quad-vacancy (Fig. 2d).

To increase the H_2 storage capacity, a maximum of four M dopants were introduced over a quad-vacancy $C_4N^{-2C/2N}$ nanosheet. The optimized structures of quad-vacancy systems functionalized with 4Li, 4Na, 4K, 4Mg, and 4Ca metals are depicted in Fig. 6. We note that the M - $C_4N^{-2C/2N}$ distances in the optimized structures are 2.04, 2.32, 2.68, 2.14, and 2.38 Å for Li, Na, K, Mg, and Ca, respectively. For comparison, the optimized minimum distances of Li-Li, Na-Na, K-K, Mg-Mg, and Ca-Ca are: 2.04, 3.34, 4.33, 2.73, and 2.86 Å, respectively. The average E_b^M per M are 3.14, 1.99, 1.93, 1.96, and 3.63 eV for Li, Na, K, Mg, and Ca, respectively, as shown in Fig. 3b. Given the strong E_b^M of M - C_4N (as compared to the corresponding E_c values) and the large M - M distances, it is evident that the M dopants are distributed uniformly over $C_4N^{-2C/2N}$ without being clustered.

The binding of metal dopants over the defected C_4N nanosheets have been verified through studying their thermal stabilities. We used the Nose-thermostat algorithm to perform ab initio molecular dynamics simulations (AIMD). Quad-vacancy nanosheets doped with four metal dopants $4MC_4N^{-2C/2N}$, are maintained at 300 K for 6 ps and the corresponding total energies are plotted versus time steps as shown in Fig. 5. Small variation in the total energies shows that the systems are thermodynamically stable.

To investigate the electronic characteristics of pristine, defected and metal functionalized systems, we have studied their electronic structures through total and partial density of states (TDOS and PDOS, respectively). Fig. 4 shows the plots of TDOS and PDOS for non-defected C_4N , and quad-vacancy $C_4N^{-2C/2N}$ nanosheets. The plots of maximum metal functionalized $4MC_4N^{-2C/2N}$ nanosheets are given in the supporting information (Figs. S1–S3). Pristine C_4N nanosheet preserves semiconducting nature with a bandgap (E_g) of 25 meV (Fig. S4 of the supporting information), which is in close agreement with the values reported by Pu and co-workers [28]. However this E_g value is underestimated due to the inability of GGA-PBE methods to calculate E_g accurately. Pu et al. have reported $E_g = 90$ meV of C_4N using the more accurate but computationally expensive hybrid method. As shown in Fig. 4a, the valence band of C_4N nanosheet is dominated by C_c (p) and N (p), whereas the conduction band is mainly contributed by C_n (p) with small contributions from C_c (p) and N (p). Introduction of vacancy defects and metal doping change the electronic properties of C_4N nanosheet. As mentioned in the above sections that various vacancy defects have been considered to improve the light metal binding over C_4N nanosheet. We describe the change in the electronic structures of C_4N upon the creation of quad vacancies ($C_4N^{-2C/2N}$) through TDOS and PDOS plots as shown in Fig. 4b. Semiconducting to metallic transition occurs in $C_4N^{-2C/2N}$. The removal of 2C and 2N from the supercell of $C_4N(C_{32}N_8)$, to form quad vacancies, results in unpaired electrons on the neighboring C and N atoms. The contribution of C_{vac} (p) and N_{vac} (p) having unpaired electrons can be seen at the top of Fermi level (E_f) in Fig. 4b. Binding of metal

dopants does not change the metallic character of the defected $C_4N^{-2C/2N}$ nanosheet, which is evident from TDOS plots of $C_4N^{-2C/2N}$ at maximum doping concentrations, that is $4MC_4N^{-2C/2N}$ (see Fig. S1 of the supporting information). To understand the bonding nature in detail, we have also plotted the PDOS plots for each of the metal doping considered in this study as shown in Figs. S2 and S3 of the supporting information. For the alkali metals, Li (s), Na (s) and K (s) it could be seen between E_f and 1.0 eV on the right of E_f . In case of alkaline metal dopants, more pronounced peaks of Mg (s) and Ca (s) are observed at E_f and in the conduction band. This could be explained due to the larger amount of charge being transferred from Mg and Ca as compared to Li, Na, and K, which is also demonstrated by Bader analysis (*vide infra*).

The bonding nature between defected $C_4N^{-2C/2N}$ nanosheet and the metal dopants can be explained through studying their charge

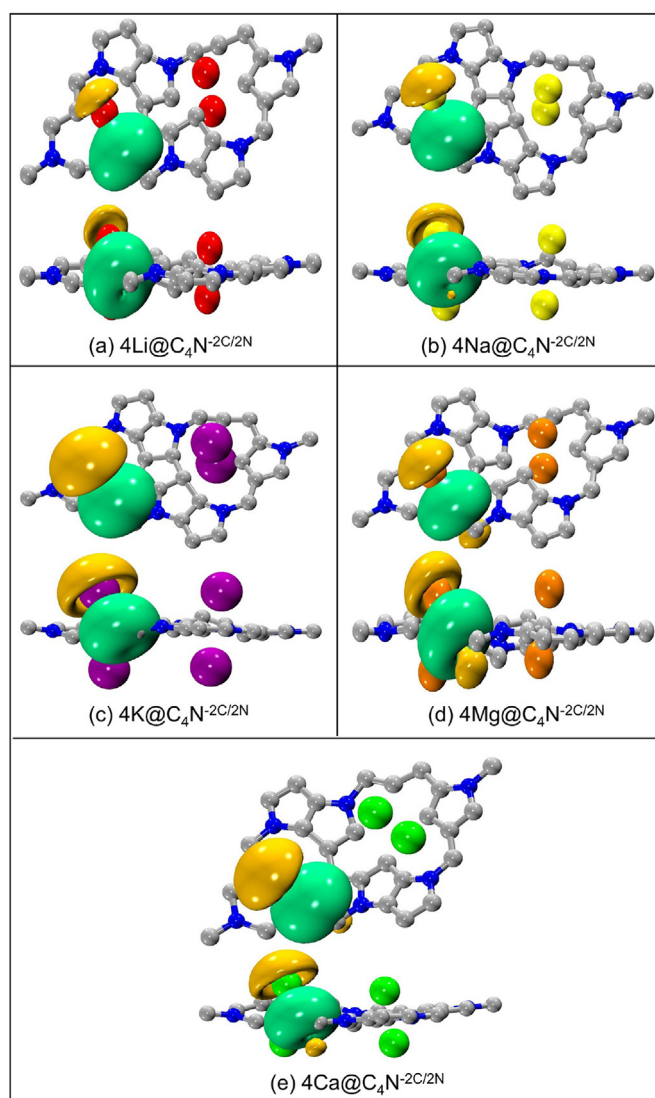


Fig. 7. Top and side views of Roby-Gould ionic orbitals for the binding between a single metal and the defected $C_4N^{-2C/2N}$ nanosheet using isovalues of ± 0.01 , ± 0.007 , ± 0.004 , ± 0.009 , and ± 0.007 for $4Li@C_4N^{-2C/2N}$, $4Na@C_4N^{-2C/2N}$, $4K@C_4N^{-2C/2N}$, $4Mg@C_4N^{-2C/2N}$, and $4Ca@C_4N^{-2C/2N}$, respectively. Green and yellow regions refer to accumulation and depletion of charges, respectively. Atom colors: C-gray, N-blue, Li-red, Na-yellow, K-purple, Mg-orange, and Ca-green. (A colour version of this figure can be viewed online.)

transfer mechanism. For this purpose, two different approaches, Bader-charge analysis (BC) [39] and Roby-Gould method (RG) [40–42], were employed to verify the direction and degree of charge transfer. Table 1 gives the total transferred charges in the valence shell of maximum M dopants (Q_{4M}), the average charges of single M (Q_M), and the maximum percentage of RG ionicity. Detailed examination of the BCs shows that each M dopant transfers a significant portion of its electronic charge to the defected $C_4N^{-2C/2N}$ nanosheet. For example, in case of a quad-vacancy sheet loaded with a maximum of four metal dopants ($4M@C_4N^{-2C/2N}$), average charges per dopant of 0.997, 0.982, 0.790, 1.842, and 1.262 are transferred to the nanosheet for Li, Na, K, Mg, and Ca, respectively. In addition, it is also evident from the isosurface charge density shown in Fig. S5 of the supporting information that charge is transferred from the M dopants to the $C_4N^{-2C/2N}$ nanosheets.

For further investigation of the binding nature, we calculated the percentage ionicity (%) of $M-C_4N^{-2C/2N}$ using the RG method, as follows,

$$\%I = 100 \times \frac{i^2}{\tau^2}. \quad (3)$$

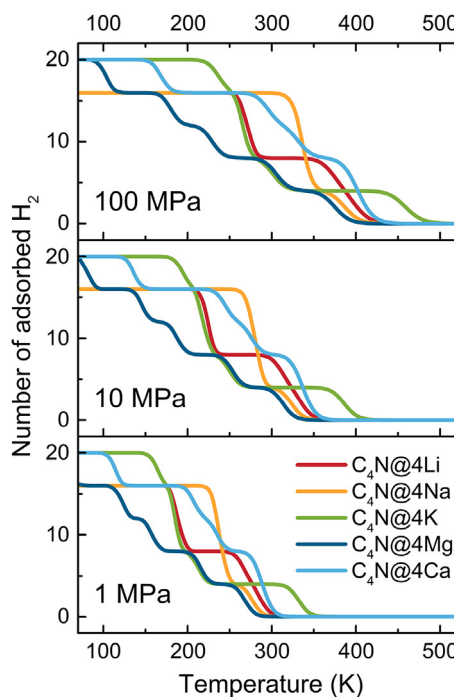
Where τ and i in the above equation are the total and ionic bond indices, respectively (more details about RG method can be found in references [40–42]). We note that the maximum %I of $M-C_4N^{-2C/2N}$ are: 64, 41, 71, 75, and 86 for the metal dopants of Li, Na, K, Mg, and Ca, respectively (Table 1). The high %I values indicate the ionic nature of the $M-C_4N^{-2C/2N}$ bonding interactions. This is further demonstrated with RG ionic orbitals (Fig. 7) showing a lower charge density around the metal dopants and an accumulated charge density around $C_4N^{-2C/2N}$ nanosheet.

In the following, we will discuss the H_2 adsorption mechanism of $4M@C_4N^{-2C/2N}$ nanosheet. Transfer of charge from M to $C_4N^{-2C/2N}$ renders the metal centers with partial positive charges ($Li^{\delta+}$, $Na^{\delta+}$, $K^{\delta+}$, $Mg^{\delta+}$, $Ca^{\delta+}$), which can polarize incoming H_2 molecules. Therefore, doped $4M@C_4N^{-2C/2N}$ sheets are able to bind H_2 significantly more strongly compared to pristine C_4N sheets. The average adsorption energies (E_{ads}) per H_2 were determined using the following equation:

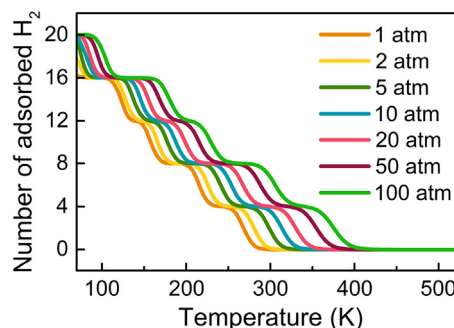
$$E_{ads} = E_{4M@C_4N^{-2C/2N}.nH_2} - E_{4M@C_4N^{-2C/2N}.(n-1)H_2} - E_{H_2}. \quad (4)$$

Where the first, second, and third terms on the right-hand-side are the total energies of decorated $4M@C_4N^{-2C/2N}$ adsorbed with n H_2 molecules, with $n-1$ H_2 molecules, and H_2 molecule, respectively. In the first step of the H_2 adsorption process, a single H_2 molecule is introduced on all active M sites of decorated $C_4N^{-2C/2N}$ nanosheet and, consequently, allow the latter to relax through structural optimization. Based on previous investigations, a vertical

interaction of H_2 with the M dopant has been shown to be more favourable compared to horizontal interaction [43]. On approaching the cationic M , adsorbed H_2 molecules are polarized and bind to the dopant through electrostatic and van der Waals forces. In order to improve the H_2 storage capacity, further H_2 molecules were inserted over the nanosheet implementing a step-wise approach. In the second step, one more H_2 molecule is introduced on each M dopant on the optimized $4H_2 - C_4N^{-2C/2N}$ system. A suitable distance between each pair of H_2 molecules was maintained in order to avoid steric repulsion between the H_2 molecules. At this stage, two H_2 molecules are bonded to each M dopant of the decorated $4M@C_4N^{-2C/2N}$ systems, resulting in adsorption of a total of $8H_2$ molecules. This process was repeated until the systems reached saturation (i.e. additional H_2 molecules were repelled by the bound H_2 molecules). Fig. 9 illustrates the hydrogenation/dehydrogenation cycle of $4K@C_4N^{-2C/2N}$ system (other decorated systems with maximum number of adsorbed H_2 molecules are given in the supporting information, Figs. S6–S9). The values of E_{ads} per H_2 and storage capacities (wt%) of $4M@C_4N$ are within the ideal range of



(a)



(b)

Table 1

Total charge transfer between the metal dopants and sheet (Q_{4M}), average charge per dopant (Q_M), and maximum Roby-Gould percentage ionicity for decorated quad-vacancy systems, $4M@C_4N^{-2C/2N}$ ($M = Li, Na, K, Mg, \text{ and } Ca$).

System	Q_{4M} (a.u.)	Q_M (a.u.)	%Ionicity
$4Li@C_4N^{-2C/2N}$	3.988	0.997	64
$4Na@C_4N^{-2C/2N}$	3.930	0.982	41
$4K@C_4N^{-2C/2N}$	3.161	0.790	71
$4Mg@C_4N^{-2C/2N}$	7.370	1.842	75
$4Ca@C_4N^{-2C/2N}$	5.047	1.262	86

Fig. 8. Adsorption/desorption process of H_2 molecules on (a) all $4M@C_4N^{-2C/2N}$, and (b) $4Mg@C_4N^{-2C/2N}$ nanosheets, as a function of pressure-temperature. M is Li, Na, K, Mg, and Ca. (A colour version of this figure can be viewed online.)

Table 2

Adsorption energies (E_{ads} in eV), H_2 storage capacity (wt%), and desorption temperature (T_D in K) for decorated systems: $nH_2-[4M@C_4N^{-2C/2N}]$, ($M = Li, Na, K, Mg,$ and Ca ; and $n = 4, 8, 12, 16, 20$).

System	E_{ads} (eV)	wt%	T_D (K)
$nH_2-[4Li@C_4N^{-2C/2N}]$			
$n = 4$	-0.303	1.67	388
$n = 8$	-0.289	3.28	370
$n = 12$	-0.240	4.84	307
$n = 16$	-0.231	6.35	296
$nH_2-[4Na@C_4N^{-2C/2N}]$			
$n = 4$	-0.289	1.48	370
$n = 8$	-0.261	2.92	334
$n = 12$	-0.255	4.32	326
$n = 16$	-0.250	5.67	320
$nH_2-[4K@C_4N^{-2C/2N}]$			
$n = 4$	-0.365	1.32	467
$n = 8$	-0.284	2.60	363
$n = 12$	-0.237	3.85	303
$n = 16$	-0.226	5.06	289
$n = 20$	-0.209	6.25	267
$nH_2-[4Mg@C_4N^{-2C/2N}]$			
$n = 4$	-0.277	1.46	354
$n = 8$	-0.242	2.88	310
$n = 12$	-0.206	4.25	264
$n = 16$	-0.177	5.59	226
$n = 20$	-0.147	6.90	188
$nH_2-[4Ca@C_4N^{-2C/2N}]$			
$n = 4$	-0.311	1.31	398
$n = 8$	-0.305	2.58	390
$n = 12$	-0.281	3.82	360
$n = 16$	-0.260	5.03	333
$n = 20$	-0.224	6.21	287

0.15–0.60 eV/ H_2 (see Table 2). Based on the above-mentioned hydrogen adsorption mechanism, we conclude that each Li or Na dopant can host a maximum of 4 H_2 molecules, i.e. a total of 16 H_2 molecules can be adsorbed on 4Li@ $C_4N^{-2C/2N}$ or 4Na@ $C_4N^{-2C/2N}$ systems. Whereas, each of the K, Mg, and Ca dopants can accommodate a maximum of 5 H_2 molecules, resulting in adsorption of a total of 20 H_2 molecules on 4K@ $C_4N^{-2C/2N}$, 4Mg@ $C_4N^{-2C/2N}$ or 4Ca@ $C_4N^{-2C/2N}$ systems (number of adsorbed H_2 molecules versus H_2 adsorption energy for all decorated systems is shown in Fig. S10 of the supporting information).

For practical H_2 storage applications, it is important to estimate the desorption temperature (T_D). We, therefore, calculate the T_D for each $nH_2-[4M@C_4N^{-2C/2N}]$ system with respect to the different number of H_2 (n) by using the van't Hoff equation [44–46];

$$T_D = \frac{E_{ads}}{k_B} \left(\frac{\Delta S}{R} - \ln p \right)^{-1} \quad (5)$$

In this equation, E_{ads} is the binding energy (in J per H_2 molecule), R is the gas constant ($8.314 \text{ J mol}^{-1} \text{ K}^{-1}$), and k_B is the Boltzmann constant ($1.380 \times 10^{-23} \text{ J K}^{-1}$). ΔS and p are the change in H_2 entropy from the gas to liquid phase ($75.44 \text{ J mol}^{-1} \text{ K}^{-1}$) and the equilibrium pressure (1 atm), respectively. Table 2 shows the values of T_D for all the decorated systems with different number of H_2 molecules. The T_D values are found to be in the range of 296–388, 320–370, 267–467, 188–354, and 287–398 for the functionalized systems of Li, Na, K, Mg, and Ca dopants, respectively. We also observe that T_D decreases with increasing number of H_2 molecules, which is expected due to lower E_{ads} values associated with a higher

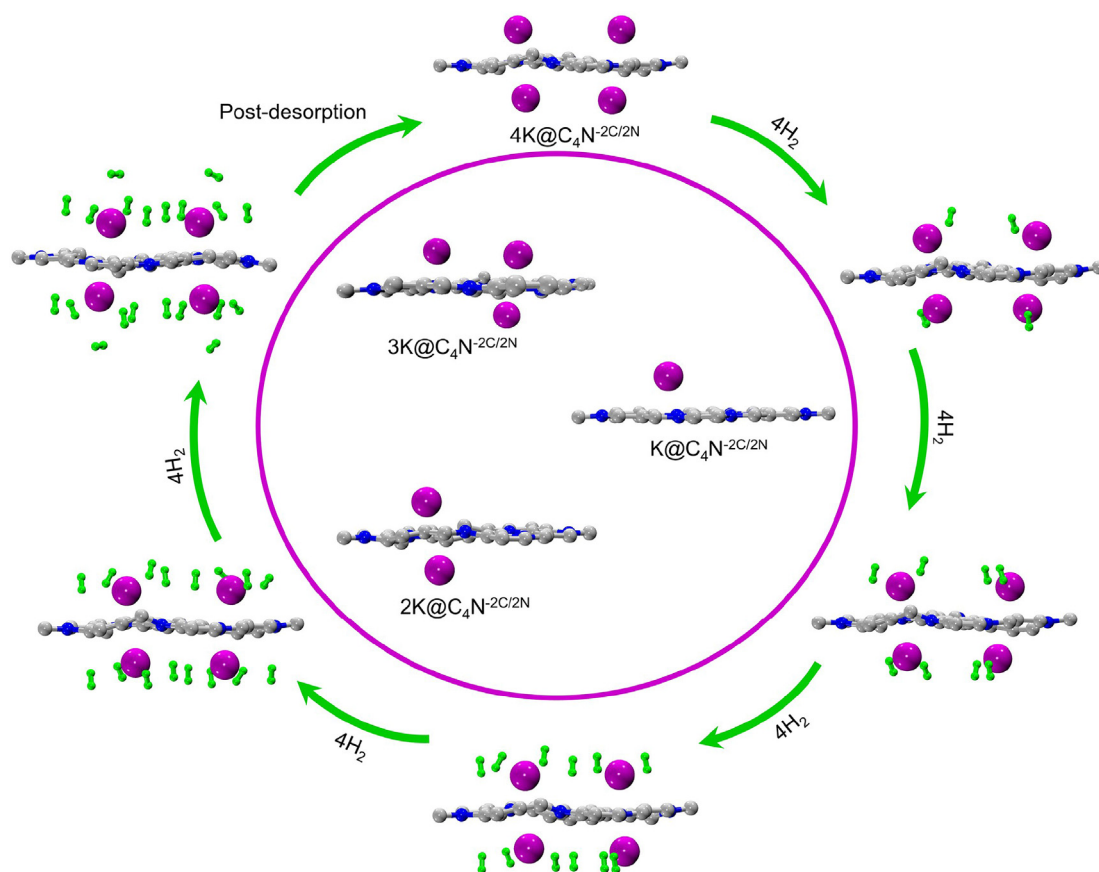


Fig. 9. Hydrogenation/dehydrogenation cycle for 4K@ $C_4N^{-2C/2N}$ (quad-vacancy) system. Optimized structures of one, two, and three K dopants over $C_4N^{-2C/2N}$ nanosheet are also given. Atom colors: C-gray, N-blue, K-purple, and H-green. (A colour version of this figure can be viewed online.)

number of adsorbed H₂ molecules.

The desorption of H₂ molecules under practical conditions is of key importance for an ideal H₂ storage nanomaterial. It is therefore important to explore H₂ storage capacity under practical pressure (P) and temperature (T) conditions. To this end, we use the thermodynamic analysis of H₂ adsorption on 4M@C₄N^{-2C/2N} nanosheets to comprehend H₂ thermodynamics at a given T and P . The number of H₂ molecules at a certain T and P ($N_{H_2}(P, T)$) was calculated using the following equation [43],

$$N_{H_2}(P, T) \equiv N_{max} \frac{\sum_{n=0}^{N_{max}} g_n e^{n(\mu - E_{ads})}}{\sum_{n=0}^{N_{max}} g_n e^{n(\mu - E_{ads})}} \quad (6)$$

Where N_{max} refers to the maximum number of H₂ molecules, the summation is over all configurations up to the N_{max} , g_n indicates the configuration multiplicity (degeneracy), and E_{ads} and μ denote the average adsorption energy per H₂ molecule and the chemical potential of the H₂ gas, respectively, for n adsorbed H₂ molecules. Fig. 8 presents the number of adsorbed H₂ molecules over 4M@C₄N^{-2C/2N} nanosheets as function of T and P . As expected, adsorption takes place at higher T when going from lower to higher P . This means that, at constant T , H₂ molecules would be released with decreasing P values. This is demonstrated in Fig. 8b of N_{H_2} on 4MgC₄N^{-2C/2N} nanosheet. Examination of both Fig. 8(a) and (b), we conclude that all M decorated nanosheets considered in this study can accommodate a reasonable number of H₂ molecules at practical T and P conditions. This further demonstrates that the C₄N^{-2C/2N} systems have the potential to become highly effective carriers of clean energy.

4. Conclusion

In conclusion, we have employed van der Waals corrected DFT calculations to investigate the H₂ storage properties of C₄N nanosheets with defects and light-metal doping. We find that pristine C₄N weakly bind the considered dopants, however the creation of vacancy defects (C-vacancy, N-vacancy, C/N di-vacancies, 2C/2N quad-vacancies) significantly improves the metal–C₄N bindings to 3–4 eV per dopant, ensuring a uniform distribution of the dopants over the nanosheet. The strong metal–C₄N bindings have been confirmed through ab initio molecular dynamics simulations at an elevated temperature of 300 K. Significant charge transfer between the metal dopants and the defected C₄N nanosheets results electronic structure changes, which have been studied through density of states calculations. We used Bader charge analysis and Roby-Gould methods for the in-depth examination of the bonding nature of metal dopants with C₄N nanosheets. The cationic metal dopants bind several H₂ molecules with adsorption energies within the ideal range of 0.15–0.50 eV/H₂ making metallized C₄N nanosheets a promising H₂ storage material. We have further employed thermodynamic analysis to study the H₂ adsorption/desorption mechanism at practical operating temperature and pressure for real world applications.

Acknowledgments

This research was undertaken with the assistance of resources provided at the NCI National Facility systems at the University of Western Australian. AK acknowledges an Australian Research Council (ARC) Future Fellowship (FT170100373). KA acknowledges the HCED in Iraq (PhD scholarship) and the University of Western Australia for Postgraduate Award. H. L. was supported by the National Institute of Supercomputing and Network/Korea Institute of Science and Technology Information with supercomputing

resources including technical support (KSC-2018-C2-0028).

Appendix A. Supplementary data

Supplementary data to this article can be found online at <https://doi.org/10.1016/j.carbon.2019.05.080>.

References

- [1] A. Schneemann, J.L. White, S. Kang, S. Jeong, L.F. Wan, E.S. Cho, T.W. Heo, D. Prendergast, J.J. Urban, B.C. Wood, et al., Nanostructured metal hydrides for hydrogen storage, *Chem. Rev.* 118 (22) (2018) 10775–10839.
- [2] M. Mananghaya, D. Yu, G.N. Santos, E. Rodolfo, Scandium and titanium containing single-walled carbon nanotubes for hydrogen storage: a thermodynamic and first principle calculation, *Sci. Rep.* 6 (2016) 27370.
- [3] A.M. Abdalla, S. Hossain, O.B. Nisfindy, A.T. Azad, M. Dawood, A.K. Azad, Hydrogen production, storage, transportation and key challenges with applications: a review, *Energy Convers. Manag.* 165 (2018) 602–627.
- [4] T. Hussain, M. Hankel, D.J. Searles, Computational evaluation of lithium-functionalized carbon nitride (g-c6n8) monolayer as an efficient hydrogen storage material, *J. Phys. Chem. C* 120 (44) (2016) 25180–25188.
- [5] R. Lavanya, V. Surya, I. Lakshmi, K. Iyakutti, V. Vasu, H. Mizuseki, Y. Kawazoe, “Hydrogen storage in tio2 functionalized (10, 10) single walled carbon nanotube (swcnt)—first principles study, *Int. J. Hydrogen Energy* 39 (10) (2014) 4973–4980.
- [6] P. Jena, Materials for hydrogen storage: past, present, and future, *J. Phys. Chem. Lett.* 2 (3) (2011) 206–211.
- [7] P. Panigrahi, A. Dhinakaran, S. Naqvi, S.G. Rao, R. Ahuja, T. Hussain, Light metal decorated graphdiyne (gdy) nanosheets for reversible hydrogen storage, *Nanotechnology* 29 (35) (2018) 355–401. IOP Publishing.
- [8] Y.-H. Kim, Y. Zhao, A. Williamson, M.J. Heben, S. Zhang, Nondissociative adsorption of h 2 molecules in light-element-doped fullerenes, *Phys. Rev. Lett.* 96 (1) (2006), 016102.
- [9] S.K. Bhatia, A.L. Myers, Optimum conditions for adsorptive storage, *Langmuir* 22 (4) (2006) 1688–1700.
- [10] US Department of Energy, Target explanation document: onboard hydrogen storage for light-duty fuel cell vehicles, technical report. available at: “, <http://energy.gov/eere/fuelcells/hydrogen-storage>.
- [11] K.S. Novoselov, A.K. Geim, S. Morozov, D. Jiang, M. Katsnelson, I. Grigorieva, S. Dubonos, Firssov, AA, Two-dimensional gas of massless Dirac fermions in graphene, *Nature* 438 (7065) (2005) 197.
- [12] Y. Zhang, Y.-W. Tan, H.L. Stormer, P. Kim, “Experimental observation of the quantum hall effect and berry’s phase in graphene, *Nature* 438 (7065) (2005) 201.
- [13] X. Yu, Z. Tang, D. Sun, L. Ouyang, M. Zhu, Recent advances and remaining challenges of nanostructured materials for hydrogen storage applications, *Prog. Mater. Sci.* 88 (2017) 1–48.
- [14] S.-Y. Cho, Y. Lee, H.-J. Koh, H. Jung, J.-S. Kim, H.-W. Yoo, J. Kim, H.-T. Jung, Superior chemical sensing performance of black phosphorus: comparison with mos2 and graphene, *Adv. Mater.* 28 (32) (2016) 7020–7028.
- [15] T. Hussain, A. De Sarkar, R. Ahuja, Functionalization of hydrogenated graphene by polythiated species for efficient hydrogen storage, *Int. J. Hydrogen Energy* 39 (6) (2014) 2560–2566.
- [16] H. Lee, W.I. Choi, M.C. Nguyen, M.-H. Cha, E. Moon, J. Ihm, Ab initio study of dihydrogen binding in metal-decorated polyacetylene for hydrogen storage, *Phys. Rev. B* 76 (19) (2007) 195110.
- [17] A.A. Ensaifi, M. Jafari-Asl, A. NABIYAN, B. Rezaei, M. Dinari, Hydrogen storage in hybrid of layered double hydroxides/reduced graphene oxide using spillover mechanism, *Energy* 99 (2016) 103–114.
- [18] T. Hussain, M. Hankel, D.J. Searles, Graphenylene monolayers doped with alkali or alkaline earth metals: promising materials for clean energy storage, *J. Phys. Chem. C* 121 (27) (2017) 14393–14400.
- [19] H.J. Hwang, Y. Kwon, H. Lee, Thermodynamically stable calcium-decorated graphyne as a hydrogen storage medium, *J. Phys. Chem. C* 116 (38) (2012) 20220–20224.
- [20] C. Zhou, J.A. Szpunar, Hydrogen storage performance in pd/graphene nanocomposites, *ACS Appl. Mater. Interfaces* 8 (39) (2016) 25933–25940.
- [21] P. Divya, S. Ramaprabhu, Hydrogen storage in platinum decorated hydrogen exfoliated graphene sheets by spillover mechanism, *Phys. Chem. Chem. Phys.* 16 (48) (2014) 26725–26729.
- [22] C. Ramos-Castillo, J. Reveles, M. Cifuentes-Quintal, R. Zope, R. de Coss, Ti4-and ni4-doped defective graphene nanoplatelets as efficient materials for hydrogen storage, *J. Phys. Chem. C* 120 (9) (2016) 5001–5009.
- [23] V.B. Parambath, R. Nagar, K. Sethupathi, S. Ramaprabhu, Investigation of spillover mechanism in palladium decorated hydrogen exfoliated functionalized graphene, *J. Phys. Chem. C* 115 (31) (2011) 15679–15685.
- [24] C. Zhou, J.A. Szpunar, X. Cui, Synthesis of ni/graphene nanocomposite for hydrogen storage, *ACS Appl. Mater. Interfaces* 8 (24) (2016) 15232–15241.
- [25] A. Hashmi, M.U. Farooq, I. Khan, J. Son, J. Hong, Ultra-high capacity hydrogen storage in a li decorated two-dimensional c 2 n layer, *J. Mater. Chem. S* 5 (6) (2017) 2821–2828.
- [26] D. Luo, J. Li, Y. Zhang, Y. Song, H. Chen, “Electronic structure and hydrogen

- storage properties of li-decorated single layer blue phosphorus, *Int. J. Hydrogen Energy* 43 (17) (2018) 8415–8425.
- [27] J. Wang, Y. Du, L. Sun, Ca-decorated novel boron sheet: a potential hydrogen storage medium, *Int. J. Hydrogen Energy* 41 (10) (2016) 5276–5283.
- [28] C. Pu, D. Zhou, Y. Li, H. Liu, Z. Chen, Y. Wang, Y. Ma, Two-dimensional c4n global minima: unique structural topologies and nanoelectronic properties, *J. Phys. Chem. C* 121 (5) (2017) 2669–2674.
- [29] G. Kresse, J. Hafner, Ab initio molecular dynamics for liquid metals, *Phys. Rev. B* 47 (1) (1993) 558.
- [30] G. Kresse, J. Hafner, “Ab initio molecular-dynamics simulation of the liquid-metal–amorphous-semiconductor transition in germanium, *Phys. Rev. B* 49 (20) (1994) 14251.
- [31] G. Kresse, J. Furthmüller, Efficient iterative schemes for ab initio total-energy calculations using a plane-wave basis set, *Phys. Rev. B* 54 (16) (1996) 11169.
- [32] J.P. Perdew, K. Burke, M. Ernzerhof, Generalized gradient approximation made simple, *Phys. Rev. Lett.* 77 (18) (1996) 3865.
- [33] P.E. Blöchl, Projector augmented-wave method, *Phys. Rev. B* 50 (24) (1994) 17953.
- [34] S. Grimme, Semiempirical gga-type density functional constructed with a long-range dispersion correction, *J. Comput. Chem.* 27 (15) (2006) 1787–1799.
- [35] H.J. Monkhorst, J.D. Pack, Special points for brillouin-zone integrations, *Phys. Rev. B* 13 (12) (1976) 5188.
- [36] R. Bader, *Atoms in Molecules: A Quantum Theory*, Oxford univ. press, , 1990.
- [37] T. Hussain, M.S. Islam, G. Rao, P. Panigrahi, D. Gupta, R. Ahuja, Hydrogen storage properties of light metal adatoms (Li, Na) decorated fluorographene monolayer, *Nanotechnology* 26 (27) (2015) 275401.
- [38] X. Zhang, C. Tang, Q. Jiang, Electric field induced enhancement of hydrogen storage capacity for Li atom decorated graphene with stone-wales defects, *Int. J. Hydrogen Energy* 41 (25) (2016) 10776–10785.
- [39] R.F. Bader, *Atoms in Molecules*, Wiley Online Library, 1990.
- [40] M.D. Gould, C. Taylor, S.K. Wolff, G.S. Chandler, D. Jayatilaka, A definition for the covalent and ionic bond index in a molecule, *Theoretical Chemistry Accounts* 119 (1–3) (2008) 275–290.
- [41] K. Alhameedi, B. Bohman, A. Karton, D. Jayatilaka, “Predicting the primary fragments in mass spectrometry using ab initio roby–gould bond indices, *Int. J. Quantum Chem.* 118 (15) (2018) 1, 1.
- [42] K. Alhameedi, A. Karton, D. Jayatilaka, S.P. Thomas, Bond orders for intermolecular interactions in crystals: charge transfer, ionicity and the effect on intramolecular bonds, *IUCrj* 5 (5) (2018) 635–646.
- [43] T. Hussain, B. Mortazavi, H. Bae, T. Rabczuk, H. Lee, A. Karton, Enhancement in hydrogen storage capacities of light metal functionalized Boron–Graphdiyne nanosheets, *Carbon* (2019).
- [44] E. Durgun, S. Ciraci, T. Yildirim, Functionalization of carbon-based nanostructures with light transition-metal atoms for hydrogen storage, *Phys. Rev. B* 77 (8) (2008), 085405.
- [45] M. Kanmani, R. Lavanya, D. Silambarasan, K. Iyakutti, V. Vasu, Y. Kawazoe, First principles studies on hydrogen storage in single-walled carbon nanotube functionalized with tio₂, *Solid State Commun.* 183 (2014) 1–7.
- [46] K. Alhameedi, A. Karton, D. Jayatilaka, T. Hussain, Metal functionalized inorganic nano-sheets as promising materials for clean energy storage, *Appl. Surf. Sci.* 471 (2019) 887–892.